npj | climate and atmospheric science

Article

Published in partnership with CECCR at King Abdulaziz University

https://doi.org/10.1038/s41612-025-01229-z

Mechanisms behind the rapid rise of extreme heat discomfort days in South China

Xin Hao[1,2,3], Huijun Wang[1,2,3], Botao Zhou[1,2,3] & Jiandong Li[4] ✉

Extreme heat discomfort days (EHDDs) are increasing in frequency and intensity under global warming, raising growing concerns in subtropical regions such as South China. Using multi-decadal observational data, we identify a marked increase in the frequency and spatial extent of EHDDs since 2000, following an absence of significant trends in earlier decades. A convolutional neural network trained on sea level pressure and 500-hPa geopotential height fields successfully detects 92% of these events and reveals their dominant circulation features. The northwestward extension of the western North Pacific subtropical high induces an anomalous anticyclone over South China, weakening summer monsoon winds and suppressing ventilation. In the presence of high humidity, these stagnant and hot conditions exacerbate heat discomfort. Concurrently, a post-2000 strengthening of mid-latitude blocking high activity reinforces high-pressure anomalies over East Asia. The joint influence of intensified blocking highs and northwestward extension of the western North Pacific subtropical high drives the sharp rise in both frequency and intensity of regional EHDDs. These findings highlight the importance of large-scale circulation changes, in combination with long-term global warming, in amplifying extreme thermal stress under a warming climate.

Outdoor heat discomfort (OHD) is an essential indicator for assessing human health and environmental conditions[1,2]. In warm seasons, a notable increase in OHD has been observed across various regions, including Asia, North Africa and Europe[3–5]. This decline may result in increased discomfort, severe heat stress, and higher health risks, especially in urban areas where heat island effects intensify these challenges for dense populations[6,7]. Furthermore, poor thermal comfort during extreme weather conditions drives substantial increases in energy demand, particularly for cooling systems, thereby amplifying energy consumption and exacerbating environmental impacts[8,9].

OHD is strongly influenced by meteorological conditions, including air temperature, humidity, wind speed, and solar radiation, with these factors interacting in a complex way to affect human physiological responses[10–12]. High humidity and stagnant winds impede sweat evaporation and convective cooling, while strong solar radiation elevates mean radiant temperature and skin heat load[13,14]. These combined effects lead to increased heat discomfort and severe health risks[13–16]. Global warming has a profound effect on OHD by altering the thermal environment in which individuals live[17–19]. Rising global air temperatures due to climate change present significant challenges for maintaining human thermal comfort outdoors (IPCC, 2021)[20]. The increased frequency and intensity of extreme heat events exacerbated discomfort and heat stress[15,21]. Although trends in relative humidity vary by region, a general pattern of decline has been observed across many land areas during boreal warm seasons, such as the Northern Hemisphere mid-latitudes, parts of South America and central Africa[22–24]. This overall decline conceals a critical health concern—high humidity levels frequently coincide with extreme heat, intensifying physiological stress and resulting in an increased number of uncomfortable days[15,25–27]. Additionally, research indicated a phenomenon known as "global terrestrial stilling," where near-surface wind speeds decreased globally by about 2.3% per

[1]State Key Laboratory of Climate System Prediction and Risk Management/Key Laboratory of Meteorological Disaster, Ministry of Education/Collaborative Innovation Center on Forecast and Evaluation of Meteorological Disasters, Nanjing University of Information Science and Technology, Nanjing, China. [2]School of Atmospheric Sciences, Nanjing University of Information Science and Technology, Nanjing, China. [3]Nansen-Zhu International Research Centre, Institute of Atmospheric Physics, Chinese Academy of Sciences, Beijing, China. [4]State Key Laboratory of Environment Characteristics and Effects for Near-space, Jiangsu Key Laboratory of Atmospheric Environment Monitoring and Pollution Control, Jiangsu Collaborative Innovation Center of Atmospheric Environment and Equipment Technology, School of Environmental Science and Engineering, Nanjing University of Information Science and Technology, Nanjing, China. ✉e-mail: lijd@nuist.edu.cn

decade from 1978 to 2010[28–30]. However, studies have noted a reversal of this trend after the year 2010, with wind speeds increasing by roughly 7% in northern mid-latitude regions[30,31]. Rising temperatures, increasing frequency of hot and humid days, and shifts in wind patterns interact to affect OHD levels.

The challenge of increasing OHD days due to rising temperatures and shifting weather patterns is an urgent issue in South China, a densely populated region highly susceptible to the impacts of climate change[3,5,25]. By the end of the century, OHD is projected to increase sharply in South China, with a significant rise in the frequency of OHD days[3,5,27]. In a warming climate, understanding how global warming impacts OHD in South China is essential not only for improving public health but also for addressing other environmental concerns, such as rising energy consumption, changes in local weather patterns, and adverse effects on mental health and social interactions.

Studies have emphasized several key large-scale circulation patterns that drive the dry or humid heat events in South China, establishing a critical connection between atmospheric dynamics and OHD variations[32–34]. These circulation patterns include the South Asian high, the western North Pacific subtropical high (WNPSH), and low-level anticyclone anomalies. Linking OHD with these circulation patterns provides a valuable framework for exploring localized climate phenomena and their driver. Recent advancements in deep learning visualization within the geosciences have opened new avenues for analyzing the dynamic processes of OHD[35–38]. In particular, convolutional neural networks (CNNs) have demonstrated strong capability in capturing complex atmospheric patterns and uncovering underlying physical processes. In this study, we implement a supervised CNN framework to identify the dominant atmospheric circulation patterns associated with extreme heat discomfort days (EHDDs) in South China. Leveraging their ability to extract spatially coherent features from gridded fields, CNNs enable recognition of key large-scale structures that drive EHDDs. This approach not only improves predictive understanding but also offers physical insights into the dynamic processes underlying EHDD occurrences within the context of global warming, contributing to more climate-resilient planning in the region.

Results

Spatial and temporal patterns of EHDDs over South China

Figure 1a illustrates the mean spatial distribution of EHDDs over South China during warm seasons from 1979 to 2023. Coastal areas and southern regions, including Hainan Island and Guangdong province, experienced the highest frequency of EHDDs, with value exceeding 70 days. Other regions such as Hunan, Jiangxi, and Guangxi provinces reported slightly fewer EHDDs, ranging between 60 and 70 days. It reveals a high prevalence of EHDDs in South China during warm seasons over the decades.

As shown in Fig. 1b, the geographical extent of EHDDs expanded significantly in South China from 1979 to 2023, particularly in the late period of 2000–2023. The affected area remained relatively stable from 1979 to 1999, showing no significant long-term trend. However, there was a significant increase in the affected areas over the period of 2000–2023. Similarly, there was a notable upward trend of 0.52 days per year ($P < 0.001$) in the frequency of regional EHDDs occurred from 1979 to 2023, with no significant trend from 1979 to 1999 and a sharper rise of 0.74 days per year ($P = 0.04$) from 2000 to 2023 (Fig. 1c). Spatial patterns of trends in the frequency of EHDDs over South China varied distinctly across the two periods. During 1979 – 1999, the frequency of EHDDs slightly increased along coastal regions of Guangdong province (Fig. 1d), whereas from 2000 to 2023, widespread increases were observed across Guangdong, Guangxi, Jiangxi, Hunan and Hainan (Fig. 1e). These regions experienced greater exposures to extreme heat discomfort, reflecting a shift from relatively stable condition pre-2000 to a pronounced rise in the frequency and intensity of EHDDs post-2000. The region's dense population further compounded the impact, as reflected in Fig. 1f, which indicates a rise in population exposure to EHDDs from 2000 to 2020.

Evaluation of the CNN

We designed a CNN to identify key circulation patterns associated with regional EHDDs (Fig. 2). The CNN model trained using SLP and 500-hPa GPH demonstrates robust performance in predicting regional EHDDs in South China (Fig. 3a). The model correctly classifies 92% of regional EHDDs as EDCPs, achieving an overall classification accuracy of 0.89 across both classes (Fig. 3b). Among all days classified as EDCPs, 58% correspond to regional EHDDs, while only 1.35% of non-EDCP days are associated with regional EHDDs. Additionally, the time series of regional EHDDs and EDCP-classified days shows a high correlation with a correlation coefficient of 0.88 (Fig. 3c), displaying the high reliability of the CNN model. With Areas under the Curve scores of 97.0% on the training set, 92.5% on the test set, and 95.9% across all days, the model strikes a good balance between precision and recall (Supplementary Fig. 4), proving its strength in

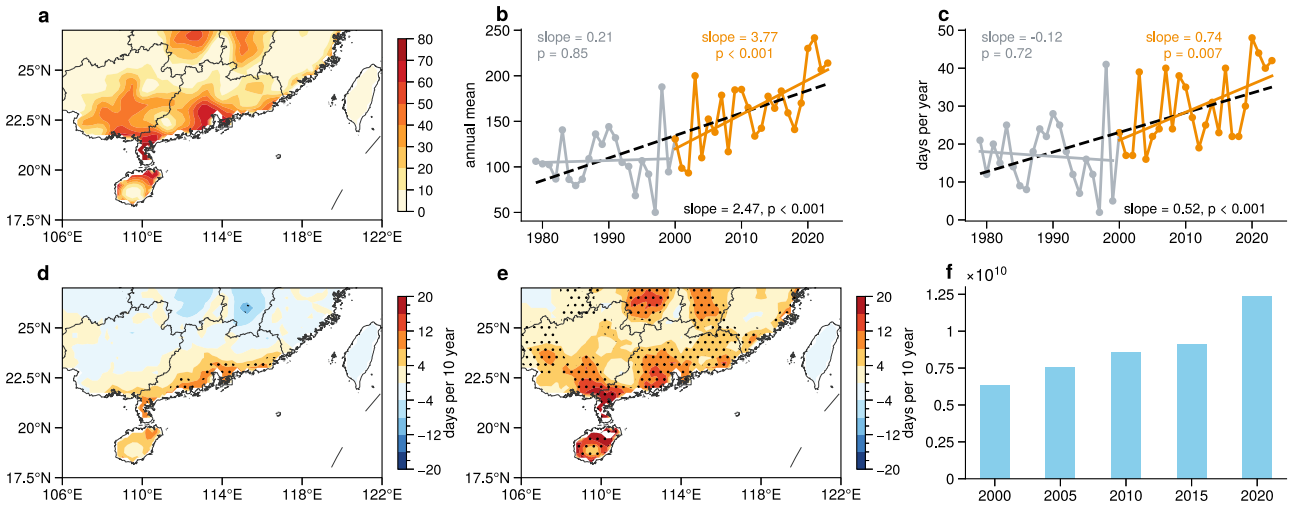

Fig. 1 | Trends and spatial patterns of extreme heat discomfort days (EHDDs) in South China. a Climatological mean frequency of EHDDs (days yr^{-1}) over South China (15°–27°N, 106°–125°E) during 1979–2023. **b** Time series of the number of grid cells affected by EHDDs, with linear trends (days yr^{-1}) for the full period (black dashed line), early period (1979–1999; gray solid line), and late period (2000–2023; orange solid line). **c** Time series of regional EHDD frequency over South China, with linear trends (days yr^{-1}) for the same three periods as in (**b**). **d**, **e** Linear trends (days per decade) in EHDDs over South China during the early (**d**) and late (**e**) periods. Dotted areas indicate regions where trends are statistically significant at the 95% confidence level (two-tailed Student's *t* test). **f** Population exposure to EHDDs in South China over time. The Breakpoint was detected using the Mann–Kendal test at the 95% confidence level.

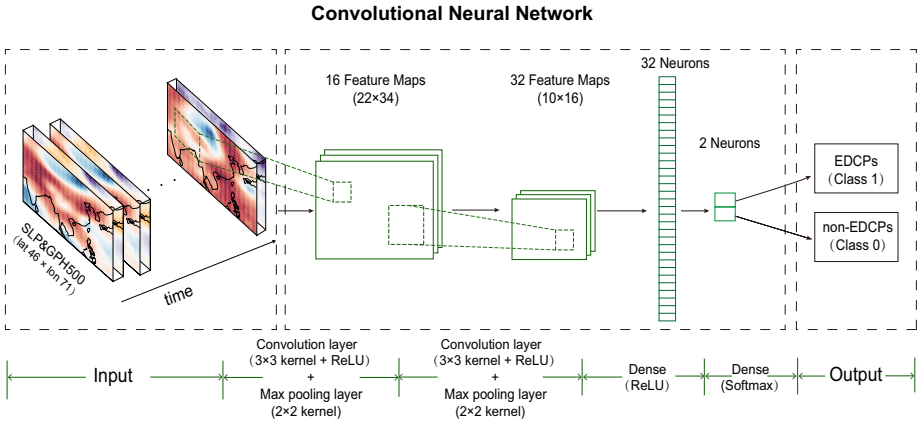

Fig. 2 | Architecture of the convolutional neural network (CNN) framework. Schematic representation of the CNN model used to identify extreme discomfort circulation patterns (EDCPs). The framework includes input preprocessing, convolutional and pooling layers, fully connected layers, and the output classification layer. The network is trained on historical atmospheric reanalysis data to detect the circulation patterns most strongly associated with extreme heat discomfort days (EHDDs) in South China.

accurately detecting the minority class EDCPs. These results suggest that the model has a strong capability to accurately recognize the minority class EDCPs.

During EDCP days, distinct atmospheric anomalies manifest in both the middle and lower troposphere. In the middle troposphere, an anticyclonic anomaly dominates South China, centered over Guangxi province, suggesting a northwestward extension of the WNPSH (Fig. 3d). Meanwhile, a cyclonic anomaly occurs at mid-latitudes around Northeast China−Korea −Japan, indicating an intensification of the East Asian westerly trough. In the lower troposphere, the SLP anomaly pattern during EDCPs show a low-pressure anomaly over the southeast of South China and a high-pressure anomaly over South Asia, accompanied by anomalous northerly winds over South China (Fig. 3d). The high-pressure anomaly over South China, resulting from the northwestward extension of the WNPSH, raises air temperatures through increased downward solar radiation and diabatic heating caused by anomalous descending air movement[39]. Moreover, anomalous northerly winds weaken the southwesterly summer monsoon, reducing wind speed over South China. As a result, increased air temperature and stagnant winds tend to trigger EHDDs. In contrast, the circulation anomaly patterns during non-EDCP days exhibit opposing characteristics, but their intensity is notably weaker compared to that for EDCP days (Fig. 3e). These non-EDCP days are associated with conditions conducive to fewer EHDD occurrences. This contrast underscores the strong influence of atmospheric circulation patterns on the CNN's ability to accurately distinguish regional EHDDs over South China.

The LRP maps provide vital insights into the features crucial for the CNN when predicting EDCPs. The normalized relevance maps exhibit physically coherent structures that align with known circulation features. Under EDCP days (Fig. 3f, g), high relevance is observed over southern and central China, and Mongolia, corresponding to regions of positive geopotential height and sea level pressure anomalies (Fig. 3d). These LRP maps indicate the model's reliance on enhanced mid- and low-level anticyclonic circulation in identifying EDCPs. In contrast, under non-EDCP days (Fig. 3h, i), the relevance patterns appear weaker and lack the coherent, organized mid-and low-latitude anomalies that characterize the composite fields (Fig. 3e). These differences suggest that the CNN learns more robust and spatially coherent circulation signals under EDCP conditions, which are more predictive of EHDD events.

Causes of changes in regional EHDDs over South China

The frequency of regional EHDDs in South China has shown a notable increase over the past decades, particularly during the period 2000–2023 (Fig. 1c). Linear trends indicate that the frequency of EDCPs increased by 0.48 days per year from 1979 to 2023 ($p < 0.01$; Fig. 3c), while regional EHDDs on EDCP days increased by 0.43 days per year during the same period ($p < 0.01$; Fig. 4a). During 2000–2023, the frequency of EDCPs significant increased at a rate of 1.03 days per year ($p = 0.002$), in contrast to the early period of 1979–1999, which exhibited an insignificant trend ($p = 0.48$; Fig. 3c). Similarly, regional EHDDs on EDCP days increased significantly in the late period by 0.52 days per year ($p = 0.04$) after a preceding period of no significant change ($p = 0.82$; Fig. 4a). Further, the intensity of extreme heat discomfort on EDCP days and the sphere of their influence were larger in the late period compared to the early period (Fig. 4b, c). Humidex values on EDCP days showed significant increases in the coastal provinces of South China (Fig. 4d–f), regions that also experienced upward trends in the frequency of EHDDs. Overall, the concurrent increases in the frequency and humidex intensity of EDCP days have contributed to the increasing frequency of regional EHDDs. The impact of EDCPs has been a key driver behind the notable shift toward more frequent and intense regional EHDDs in South China over recent decades.

On average, EDCP days were characterized by heat discomfort due to a combination of high air temperature and high relative humidity (Fig. 5a, c). Although relative humidity values are slightly higher on non-EDCP days by approximately 5% (Fig. 5b vs. a), both EDCP and non-EDCP days show generally high relative humidity (65–95%). However, EDCP days exhibit significantly higher temperatures, frequently exceeding 27 °C and in some instances surpassing 29 °C, whereas non-EDCP days remain distinctly cooler (Fig. 5c, d). In the late period, EDCPs show increasing humidex intensity and spatial expansion of EHDDs, which coincide with the region with strong warming and drying (Fig. 5a, c, right panels), indicating a worsening trend in heat stress. Further, the lower wind speeds over South China in the late period intensified the thermal stress on EDCP days (Fig. 5e). In contrast, non-EDCP days reveal lower air temperature despite a general increase in air temperature during the late period (Fig. 5b). Despite the slight decline in relative humidity over most regions of South China across both categories, the effect of rising temperature appears to be the dominant driver of intensifying EHDD conditions over South China.

To identify the causes of changes in relative humidity and air temperature, differences in atmospheric circulation patterns between the late and early periods were analyzed. During EDCP days, the WNPSH shows a northwestward extension relative to climatology, while in the late period, compared to the early period, the WNPSH exhibits a westward extension (Fig. 6a vs. b). These features jointly indicate that the WNPSH has shifted both westward in recent decades and northward during EDCP events. Meanwhile, results reveal a strengthening of mid-latitude high-pressure anomalies during the 2000–2023 period, particularly during EDCP days (Fig. 6a, b). On EDCP days, stronger blocking high anomalies at mid-latitudes were observed in the late period compared to the early period (Fig. 6b, d). The intensity of these blocking high shows a significant increase and is strongly correlated with the frequency of regional EHDDs, with a

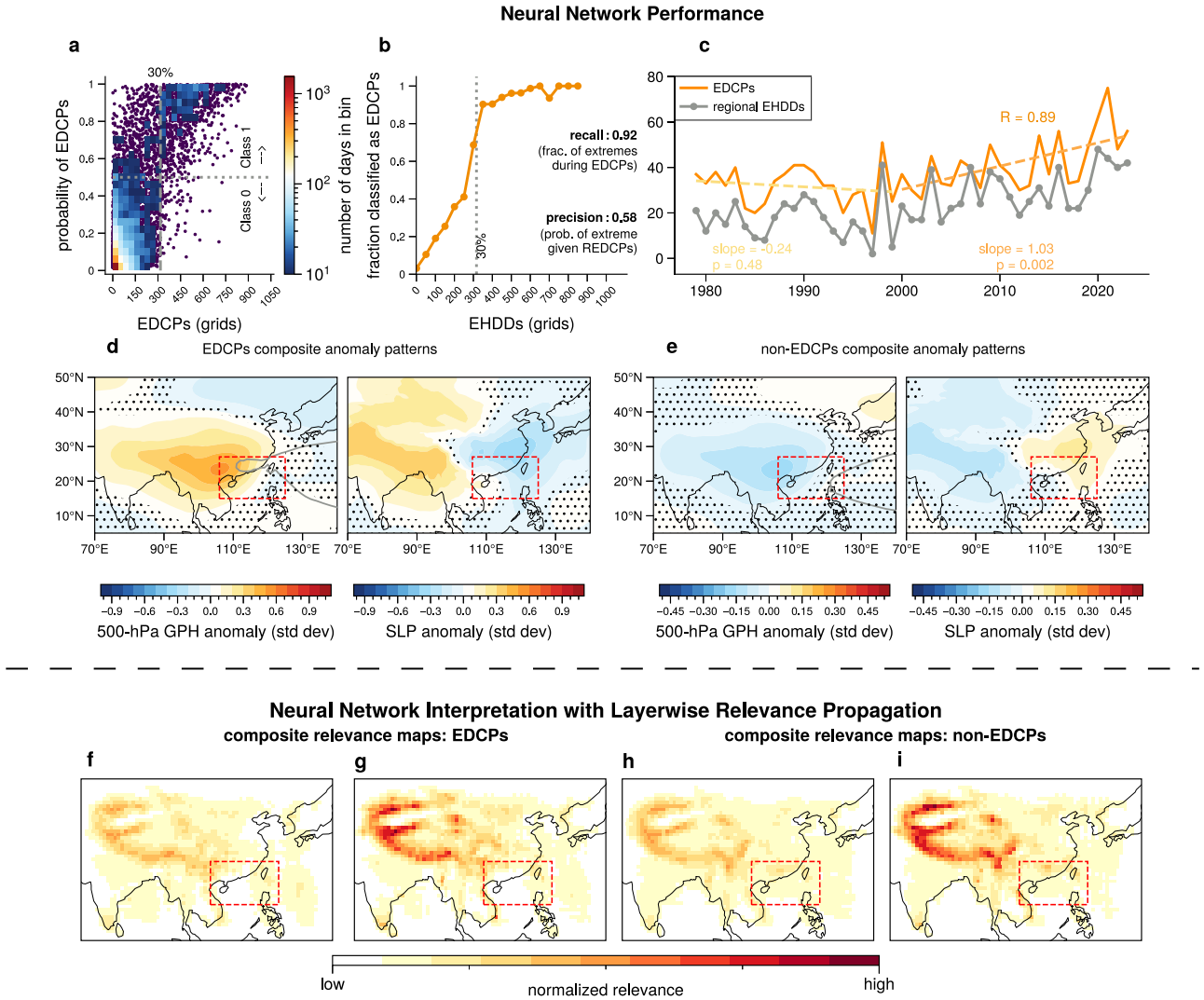

Fig. 3 | Neural network classification and circulation characteristics of extreme discomfort circulation patterns (EDCPs). a Joint distribution of the number of extreme heat discomfort grids and the predicted EDCP probability for each day. Color shading ($\log_{10}$ scale) indicates the number of days in each bin; individual days are shown as dots. The vertical dashed line marks the 30% threshold used to define regional extreme heat discomfort days (EHDDs). **b** Fraction of days classified as EDCPs for different levels of EHDD-affected grid cell counts. **c** Time series of regional EHDD frequency (gray line) and EDCP frequency, with linear trends ($days\ yr^{-1}$) in EDCP frequency for the early (1979–1999; light orange dashed line) and late periods (2000–2023; orange dashed line). **d**, **e** Composite anomaly maps of atmospheric variables for EDCP (**d**) and non-EDCP (**e**) days. **f**–**i** Layer-wise relevance propagation (LRP) composite maps highlighting relevant input regions for CNN-predicted EDCP and non-EDCP events. Dotted areas in **d** and **e** indicate regions where changes are not statistically significant at the 95% confidence level (two-tailed Student's *t* test). The gray contours in d and e indicate the 5870-m geopotential height.

correlation coefficient of 0.6 during the late period, whereas no clear trend is found during the early period (Fig. 6f). These blocking high anomalies favored anticyclonic anomalies co-occur with stronger anticyclonic anomalies over South China that associated with the northwestward extension of the WNPSH in low latitudes (Fig. 6d). Such circulation anomalies can obstruct the typical movement of weather systems and promote atmospheric stagnation, leading to persistent subsidence that inhibits cloud formation, enhances solar radiation, and thereby amplifies surface warming[40–44]. In addition, blocking highs in mid-latitudes of East Asia can hinder the southward intrusion of cooler air, trapping heat near the surface and contributing to the buildup of extreme temperatures in South China[40,43]. These co-occurring circulation features match those identified as important by the CNN model for predicting EDCPs (Fig. 3h, i), supporting their role in increasing EDCP occurrences. Taken together, the notable strengthening of mid-latitude blocking high activity since 2000 may be a major contributor to the rising frequency of regional EHDDs in South China (Fig. 6f), while both intensified blocking highs and global warming jointly contribute to the observed rise in EHDDs intensity across the region.

Discussion

In recent decades, South China has experienced a significant increase in regional EHDDs during warm seasons, marking a notable shift from relatively stable conditions pre-2000 toward a pronounced intensification of extreme heat discomfort events that affect millions of residents across the region. While no significant trend was observed from 1979 to 1999, the subsequent period from 2000 to 2023 demonstrates dramatic changes, with a significant upward trend in both frequency and spatial extent of these events. Spatially, increases were initially confined to the coastal area of Guangdong, but later expanded to multiple provinces, including Guangdong, Guangxi, Jiangxi, Hunan, and Hainan.

CNN analysis of atmospheric circulation patterns associated with regional EHDDs identifies the northwestward extension of the WNPSH as a primary driver. The northwestward extension induces an anomalous anticyclone over South China, leading to a weakened summer monsoon and

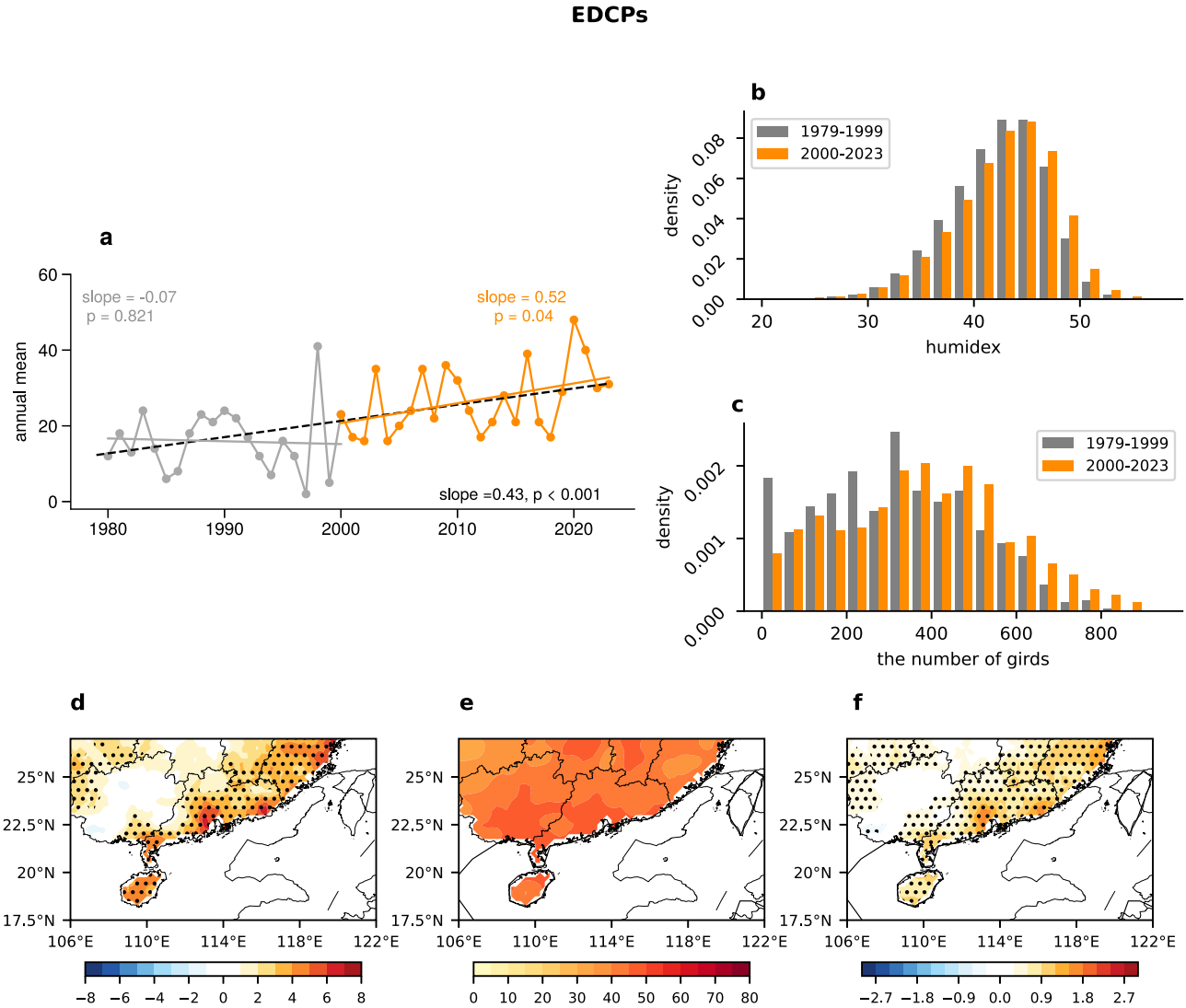

Fig. 4 | Changes in extreme heat discomfort characteristics associated with EDCP days in South China. a Time series of regional extreme heat discomfort days (EHDDs) during EDCP days, with linear trends (days yr^{-1}) for the full period (black dashed line), early period (1979–1999; gray solid line), and late period (2000–2023; orange solid line). **b** Distribution of daily humidex values during EDCP days for the early and late periods. **c** Distribution of the number of daily affected grid cells during EDCP days for the early and late periods. **d** Linear trend in mean humidex during EDCP days for 1979–2023. **e** Climatological mean humidex during EDCP days (1979–2023). **f** Difference in mean humidex between the late and early periods (2000–2023 minus 1979–1999). Dotted areas in e and f indicate regions with statistically significant changes at the 95% confidence level (two-tailed Student's *t* test).

increased surface air temperatures. The combination of stagnant winds, high temperatures, and the naturally high humidity of the region creates conditions conducive to extreme heat discomfort. Despite advancements in understanding circulation patterns associated with regional EHDDs, some extreme heat discomfort events with "atypical" circulation patterns remain challenging for current models to capture (Supplementary Fig. 6). This limitation may be attributed to variations in the spatial distribution of regional extreme heat discomfort events or the intricate balance among temperature, humidity, and wind factors influencing heat discomfort levels. Addressing these challenges in future research is essential to improve the CNN model's ability to better predict and analyze these atypical events.

During 2000–2023, blocking highs anomalies at mid-latitudes have become increasingly prevalent, resulting in enhanced high-pressure anomalies over the East Asian continent that favor the occurrence of EDCPs. The synergistic effect of the northwestward extension of the WNPSH and mid-latitude blocking highs has emerged as the dominant driver of the increased frequency of regional EHDDs in South China since 2000. The intensification of mid-latitude blocking high events appears to be associated with broader climate change patterns[45,46], such as Arctic amplification and sea-ice decline[47–51]. Francis and Vavrus[51] suggest that Arctic amplification weakens the equator-to-pole temperature gradient, thereby slowing the westerly jet stream and increasing the frequency of strong blocking events. Of particular significance is the shift in the trend of Russian Arctic sea-ice around the year 2000—from a period of no significant trend to a period of rapid decline, which has coincided with increasingly persistent and stronger summer blocking events over eastern Siberia due to smaller meridional potential vorticity gradients under reduced sea-ice conditions[47–49]. Another prominent factor potentially contributing to the increased regional EHDDs in South China is the Pacific decadal oscillation. The mid-1990s phase shift of the Pacific decadal oscillation from positive to negative, along with the phase shift of the Atlantic multidecadal oscillation from negative to positive, has been linked to an intensified northern branch wave train over Eurasia. This strengthened wave train enhances geopotential height anomalies over the Ural Mountains and eastern Siberia, forming favorable conditions for the occurrence of blocking high at mid-latitudes during summer[52–55]. Understanding these connections provides valuable insight into the mechanisms driving extreme heat discomfort events in South China, with implications for improving prediction and preparedness for heat-related health risks.

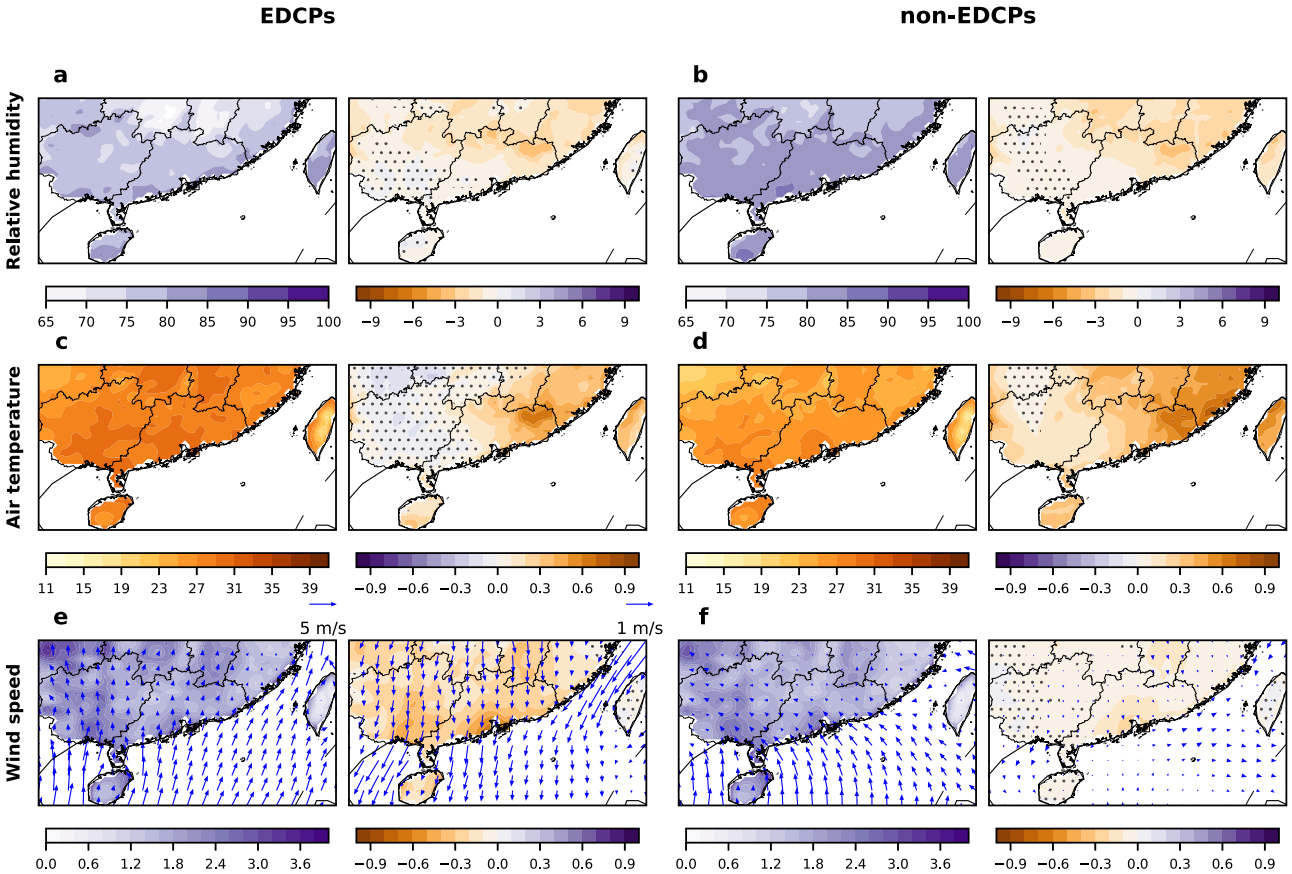

Fig. 5 | Surface meteorological conditions associated with extreme discomfort circulation pattern (EDCP) and non-EDCP days. a Composite of relative humidity (shading; %) on EDCP days during the full period, along with differences between the late and early periods. Dotted areas indicate regions where changes are not statistically significant at the 95% confidence level (two-tailed Student's *t* test). **b** Same as **a**, but for non-EDCP days. **c**, **d** Same as (**a**, **b**), respectively, but for 2-m air temperature (°C). **e**, **f** Same as (**a**, **b**), respectively, but for near-surface wind speed (m s^{-1}) and near-surface wind vectors (m s^{-1}).

In addition to these large-scale circulation drivers, the role of long-term global warming cannot be overlooked. Both EDCP days and non-EDCP days exhibit significant warming, emphasizing the critical role of long-term global warming in driving temperature increases (Fig. 5c, d). The positive trend in air temperature is attributable not only to greenhouse gas-induced warming but also to intensified urbanization at the regional scale[56,57]. These anthropogenic influences may act in concert with circulation anomalies to exacerbate the frequency and intensity of EHDDs in the region. While our findings suggest a strong dynamical connection between mid-latitude blocking highs, the WNPSH, and EHDDs in South China, the attribution of EHDDs to specific circulation patterns may also be influenced by concurrent global warming trends. Future studies employing climate model experiments are needed to rigorously assess the underlying causal mechanisms.

Methods

Observational datasets and OHD index

To quantify OHD under extreme heat and humidity, we employ the humidex index, a widely used measure adopted by previous studies[10,58]. The humidex combines air temperature (T, in °C) and dew point temperature (T_{dew}, in °C) into a single value representing the perceived temperature. Its effectiveness has been demonstrated in public health and heat stress studies across humid regions, including South China[59,60]. The formulation is expressed as:

$$H = T + 0.5555\left[6.11e^{5417.753\left(\frac{1}{273.16}-\frac{1}{273.16+T_{dew}}\right)} - 10\right] \quad (1)$$

Here, the coefficient 5417.753 is derived from the Clausius-Clapeyron relation and reflects the laten heat of vaporization, the universal gas constant, and the molecular weight of water. The constant 273.16 is the melting point of ice in Kelvin.

For humidex, we use the gridded daily observational dataset obtained from CN05.1[61]. Because T_{dew} is not directly available in CN05.1 dataset, we calculate it iteratively from air temperature and relative humidity as follow. First, the saturation vapor pressure (e_s) is computed based on the air temperature (T, in K) using the formula:

$$e_s = 6.1078e^{\left[\frac{a(T-273.16)}{T-b}\right]} \quad (2)$$

where constants a and b adjusted based on the temperature range. For a $T \geq 258.16$ K, $a = 17.27$, **b** = 35.86; for $T \leq 233.16$ K, $a = 21.87$, $b = 7.66$; and for 233.16 K ≤ T ≤ 258.16 K, a and b are interpolated linearly.

Next, the actual vapor pressure (e) is obtained from the relative humidity (RH, in %) using:

$$e = \frac{e_s RH}{100} \quad (3)$$

Finally, to determine T_{dew}, we iteratively decrease T in 0.05 K increments and recalculate e_s until $e = e_s$. The temperature satisfying this condition is taken as the dew point temperature T_{dew}.

For atmospheric field, we use the daily fifth-generation ECMWF reanalysis (ERA5) dataset[62], including sea level pressure (SLP), zonal and meridional winds at 10 m, relative humidity, air temperature at 2 m, geopotential height (GPH) at 500-hPa. The analysis focuses on warm months

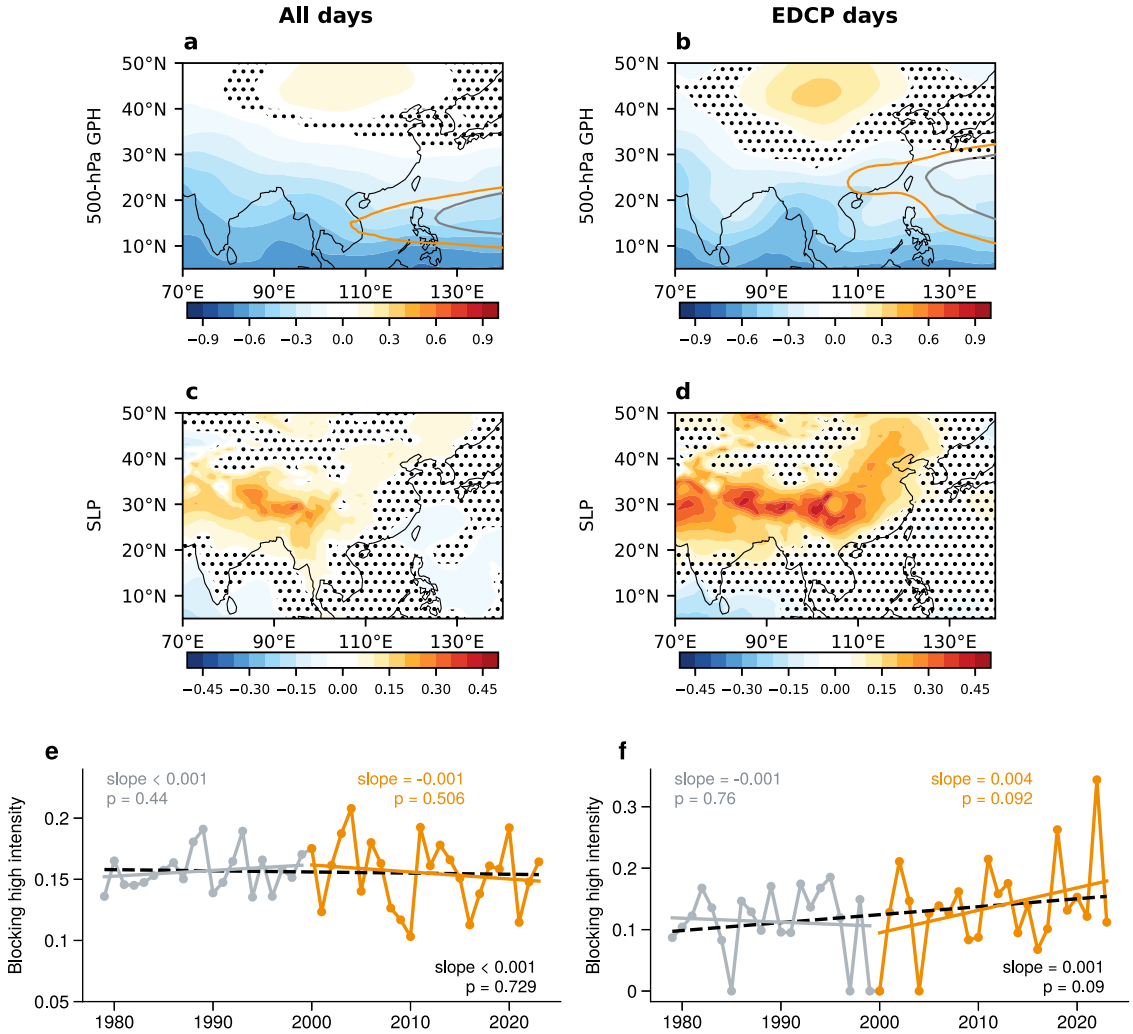

Fig. 6 | Atmospheric circulation anomalies associated with extreme heat discomfort in South China. a Differences in 500-hPa geopotential height (shading; m) between the late and early periods across all summer days. The orange contours indicate the 5870-m geopotential height during the late period (2000 − 2023), while gray contours denote the 5870-m geopotential height during the early period (1979 − 1999). Dotted areas denote regions where differences are not statistically significant at the 95% confidence level (two-tailed Student's *t* test). **b** Same as (**a**), but for days classified as extreme discomfort circulation pattern (EDCP) days. **c**, **d** Same as (**a**, **b**), respectively, but for sea level pressure anomalies (shading; hPa). **e** Time series of annual mean blocking high intensity across all summer days, with linear trend (m yr^{-1}) for the full period (black dashed line), early period (1979–1999; gray solid line), and late period (2000–2023; orange solid line). **f** Same as (**e**), but for EDCP days.

(May−September) from 1979 to 2023, during which both the CN05.1 and ERA5 reanalysis datasets are available. The CN05.1 data are used at a 0.25° × 0.25° spatial resolution. For ERA5, SLP and 500-hPa GPH are used at 1° × 1°, while 10 m wind, 2 m temperature, and relative humidity are used at 0.25°° × 0.25°. Additionally, the Gridded Population of the World version 4[63] dataset provides population counts at a 0.25° × 0.25° resolution for 2000, 2005, 2010, 2015 and 2020 to assess population exposure.

In this study, we focus on South China (15°N to 27°N, 106°E to 125°E). Heat discomfort is classified as extreme when the humidex exceeds 45, signifying dangerous conditions with an elevated risk of heat stroke. EHDDs are defined as those humidex values exceeding 45 for a specific grid, and regional EHDDs occur when 30% or more of grids exceed a humidex value of 45. Results remain robust across alternative thresholds (35% and 40%), yielding similar trends in regional EHDDs, classification performance, and circulation composites (Supplementary Figs. 1–3).

Detection of atmospheric blocking

To examine the role of mid-latitude blocking high in driving EHDDs in South China during summer, we adopt a 500-hPa GPH-based blocking detection and intensity quantification approach. Blocking events are identified using a modified version of the classical Tibaldi and Molteni[64] method, which detects persistent high-pressure anomalies in the mid-troposphere based on meridional GPH gradients. A given longitude λ is considered to exhibit blocking on a particular day if the following two gradient conditions are simultaneously satisfied for at least one value of Δ :

$$\begin{cases} GHG_N(\lambda) = \frac{GPH(\lambda,\phi_N) - GPH(\lambda,\phi_0)}{\phi_N - \phi_0} < -\frac{10m}{deglat} \\ GHG_S(\lambda) = \frac{GPH(\lambda,\phi_0) - GPH(\lambda,\phi_S)}{\phi_0 - \phi_S} > 0 \end{cases} \quad (4)$$

Here, $\phi_N = 75^\circ + \Delta, \phi_0 = 60^\circ + \Delta, \phi_S = 40^\circ + \Delta$, with $\Delta = -5^\circ, -2.5^\circ, 0^\circ, 2.5^\circ, 5^\circ$. The central ($\phi_0$) and the southern ($\phi_S$) points are set at 60° and 40° based on previous studies[65,66], while the northern point is adjusted to 75° (instead of the original 80°) to better capture blocking patterns relevant to the southern focus of this study[67]. We define a blocking day if blocking is detected over at least 13 consecutive degrees of longitude within the domain $\lambda \in [80^\circ E, 130^\circ E]$. The longitudinal range covers the region where strong positive geopotential height anomalies are frequently observed (Figs. 2d and 6b, d). This spatial extent corresponds approximately to the longitudinal

range centered on Lake Baikal (~ 108°E), and the 13-degree threshold reflects adaptation to the 1° resolution of ERA5 reanalysis data (compared to 12.5° used in coarser-resolution studies).

The blocking center point ($\lambda_{ctr}, \phi_{ctr}$) is identified as the grid point with the largest zonally and meridionally averaged 500-hPa GPH anomaly within a reference region. This reference region is defined by extending 5° east and west from the easternmost and westernmost boundaries of the blocking ridge. The blocking intensity (BI) is then computed as[68]:

$$BI = 100 \times \left(\frac{GPH(\lambda_{ctr}, \phi_{ctr})}{GPH_{ref}} - 1.0 \right) \quad (5)$$

where GPH_{ref} is the mean 500-hPa GPH at the upstream (λ_{up}) and downstream (λ_{down}) boundaries of the blocking region, defined as:

$$GPH_{ref} = \frac{1}{2}\left[GPH\left(\lambda_{up}, \phi\right) + GPH\left(\lambda_{down}, \phi\right) \right] \quad (6)$$

High BI values indicate stronger blocking highs.

CNN architecture for identifying extreme discomfort circulation patterns (EDCPs)

In training a CNN to predict regional EHDDs in South China, we use daily SLP and 500-hPa GPH anomalies for the geographic domain spanning 5°N to 50°N and 70°E to 140°E. Including 250-hPa zonal wind as an additional predictor does not improve performance, and using 500-hPa GPH alone leads to substantially worse results (Supplementary Fig. 4). Before analysis, both SLP and 500-hPa GPH anomalies are standardized, and the area-weighted average trend over the atmospheric domain is removed from GPH values to adjust for uniform thermal expansion. The dataset is split into training (75%) and testing (25%) subsets for model development and evaluation. During training, days identified as regional EHDDs are labeled as class 1, while non-regional EHDDs are labeled as class 0. This classification approach enables the model to effectively learn the distinguishing circulation features associated with regional extreme heat discomfort. After training, the trained model processes the standardized SLP and 500-hPa GPH anomaly patterns as three-dimensional input data to predict the probability of each day from 1979 to 2023 being associated with a regional EHDD-related circulation pattern. A prediction probability exceeding 0.5 is classified as an extreme discomfort circulation pattern (EDCP), while lower probabilities indicate non-EDCPs. To ensure robustness, we tested alternative thresholds (0.4, 0.6) and found consistent classification performance (Supplementary Fig. 5).

The CNN architecture (Fig. 2) consists of two convolutional layers aimed at feature extraction and transformation. The first layer utilizes 16 filters, while the second layer employs 32 filters, with both layers featuring a 3×3 kernel and using ReLU activation for non-linearities. These layers are followed by two max pooling layers with 2×2 kernels, which are responsible for feature extraction and dimensionality reduction. The output of the convolutional and pooling layers is then flattened and processed through two fully connected dense layers for classification. The first dense layer contains 32 neurons with ReLU activation, ensuring complex non-linear feature representation. The second dense layer consists of 2 neurons and employs softmax activation, which converts the outputs into probabilities for EDCP classification. To optimize the performance and generalization of the CNN, the architecture is fine-tuned with several critical hyperparameters, including a learning rate of 2×10^{-4}, a batch size of 2048, L2 regularization rates of 1×10^{-2}, 7×10^{-4} and 1×10^{-4}, and a dropout rate of 0.1. Weight initialization is handled with a random normal initializer. More details on the CNN are shown in the supplementary.

Layer-wise relevance propagation (LRP)

A CNN transforms input features into abstracted, higher-level representations, which complicates direct interpretation of how specific input features contribute to the final prediction. LRP has been widely used in previous studies[35,69,70] as a useful tool to enhance interpretability in deep learning models. LRP propagates the model's output backward through the network layers, redistributing the prediction score to the input features based on the network's structure and weights. In doing so, it reveals the contributions of each input feature to the model's decision and provides insights into the mechanisms driving the predictions. Following Davenport and Diffenbaugh[35] and Montavon, Samek[69], we adopt the LRP technique by setting the parameters $\alpha = 1$ and $\beta = 0$ to explain the predictions of neural networks. This particular configuration emphasizes highlighting the relevant features of input data by assigning them positive relevance scores. Given the variability in model output magnitude across samples—even within the same predicted class—we normalized the relevance scores for each sample before compositing. This normalization step ensures that the relevance maps reflect the relative importance of input features across space, rather than absolute output strength, and enables meaningful interpretation of the spatial relevance patterns. By focusing on normalized relevance within each class (EDCP vs. non-EDCP), our interpretation highlights how the model prioritizes specific spatial features for classification.

Data availability

The ERA5 dataset is available from https://cds.climate.copernicus.eu/datasets/reanalysis-era5-single-levels?tab=overview. The CN05.1 dataset used in this study is not publicly accessible but can be obtained from the corresponding author on reasonable request.

Code availability

The code used for data analysis is available upon request.

Received: 24 April 2025; Accepted: 6 September 2025;
Published online: 23 October 2025

References

1. Nikolopoulou, M. & Steemers, K. Thermal comfort and psychological adaptation as a guide for designing urban spaces. *Energy Build.* **35**, 95–101 (2003).
2. Honjo, T. Thermal comfort in outdoor environment. *Glob. Environ. Res.* **13**, 43–47 (2009).
3. Li, W. et al. Detection and attribution of changes in thermal discomfort over China during 1961–2014 and future projections. *Adv. Atmos. Sci.* **39**, 456–470 (2022).
4. Cheung, C. S. C. & Hart, M. A. Climate change and thermal comfort in Hong Kong. *Int. J. Biometeorol.* **58**, 137–148 (2014).
5. Li, W. & Hao, X. Attribution analysis of human discomfort days in the Northern Hemisphere and their prediction in the future. *Trans. Atmos. Sci.* **46**, 14 (2023).
6. Ren, J., Shi, K., Li, Z., Kong, X. & Zhou, H. A review on the impacts of urban heat islands on outdoor thermal comfort. *Buildings* **13**, 1368 (2023).
7. Xi, C., Ren, C., Wang, J., Feng, Z. & Cao, S.-J. Impacts of urban-scale building height diversity on urban climates: a case study of Nanjing, China. *Energy Build.* **251**, 111350 (2021).
8. Khraiwesh, M. M. & Genovese, P. V. Outdoor thermal comfort integrated with energy consumption for urban block design optimization: a study of the hot-summer mediterranean city of Irbid, Jordan. *Sustainability* **15**, 8412 (2023).
9. Li, J. & Liu, N. The perception, optimization strategies and prospects of outdoor thermal comfort in China: a review. *Build. Environ.* **170**, 106614 (2020).
10. Zhu, J., Wang, S. & Huang, G. Assessing climate change impacts on human-perceived temperature extremes and underlying uncertainties. *J. Geophys. Res. Atmos.* **124**, 3800–3821 (2019).
11. Li, J., Chen, Y. D., Gan, T. Y. & Lau, N.-C. Elevated increases in human-perceived temperature under climate warming. *Nat. Clim. Change* **8**, 43–47 (2018).

12. Ma, W. et al. The temperature–mortality relationship in China: an analysis from 66 Chinese communities. *Environ. Res.* **137**, 72–77 (2015).
13. Huang, X., Yao, R., Xu, T. & Zhang, S. The impact of heatwaves on human perceived thermal comfort and thermal resilience potential in urban public open spaces. *Build. Environ.* **242**, 110586 (2023).
14. Xu, Z., FitzGerald, G., Guo, Y., Jalaludin, B. & Tong, S. Impact of heatwave on mortality under different heatwave definitions: a systematic review and meta-analysis. *Environ. Int.* **89-90**, 193–203 (2016).
15. Fischer, E. M. & Schär, C. Consistent geographical patterns of changes in high-impact European heatwaves. *Nat. Geosci.* **3**, 398–403 (2010).
16. Knowlton, K. et al. The 2006 California heat wave: impacts on hospitalizations and emergency department visits. *Environ. Health Perspect.* **117**, 61–67 (2009).
17. Zhang, J. et al. Inequality of global thermal comfort conditions changes in a warmer world. *Earth's. Future* **11**, e2022EF003109 (2023).
18. Kjellstrom, T., Holmer, I. & Lemke, B. Workplace heat stress, health and productivity – an increasing challenge for low and middle-income countries during climate change. *Glob. Health Action* **2**, 2047 (2009).
19. Sailor, D. J., Baniassadi, A., O'Lenick, C. R. & Wilhelmi, O. V. The growing threat of heat disasters. *Environ. Res. Lett.* **14**, 054006 (2019).
20. Masson-Delmotte V. et al. Ipcc, 2021: Summary for policymakers. In: Climate change 2021: The physical science basis. contribution of working group i to the sixth assessment report of the intergovernmental panel on climate change. https://www.ipcc.ch/report/ar6/wg1/ (2021).
21. Russo, S., Sillmann, J. & Sterl, A. Humid heat waves at different warming levels. *Sci. Rep.* **7**, 7477 (2017).
22. Vicente-Serrano, S. M. et al. Recent changes of relative humidity: regional connections with land and ocean processes. *Earth Syst. Dyn.* **9**, 915–937 (2018).
23. Willett, K. M. et al. HadISDH land surface multi-variable humidity and temperature record for climate monitoring. *Clim.***10**, 1983–2006 (2014).
24. Simmons, A. J., Willett, K. M., Jones, P. D., Thorne, P. W., Dee, D. P. Low-frequency variations in surface atmospheric humidity, temperature, and precipitation: Inferences from reanalyses and monthly gridded observational data sets. *J. Geophys. Res. Atmos.* **115** (2010).
25. Qiao, N. et al. Trend, driving factors, and temperature-humidity relationship of the extreme compound hot and humid events in South China. *Theor. Appl. Climatol.* **155**, 4213–4230 (2024).
26. He, W., Chen, H. & Ma, J. Variations in summer extreme hot–humid events over Eastern China and the possible associated mechanisms. *J. Clim.* **36**, 3801–3815 (2023).
27. Wei, Y. et al. Climate change dominates the increasing exposure of global population to compound heatwave and humidity extremes in the future. *Clim. Dyn.* **62**, 6203–6217 (2024).
28. Xu, C. -y, Gong, L., Jiang, T., Chen, D. & Singh, V. P. Analysis of spatial distribution and temporal trend of reference evapotranspiration and pan evaporation in Changjiang (Yangtze River) catchment. *J. Hydrol.* **327**, 81–93 (2006).
29. Roderick, M. L., Rotstayn, L. D., Farquhar, G. D. & Hobbins, M. T. On the attribution of changing pan evaporation. *Geophys. Res. Lett.* **34** (2007).
30. Zeng, Z. et al. A reversal in global terrestrial stilling and its implications for wind energy production. *Nat. Clim. Change* **9**, 979–985 (2019).
31. Zhou, L. et al. A continuous decline of global seasonal wind speed range over land since 1980. *J. Clim.* **34**, 9443–9461 (2021).
32. Wu, X. et al. Influence of large-scale circulation patterns on compound dry and hot events in China. *J. Geophys. Res. Atmos.***126**, e2020JD033918 (2021).
33. Luo, M., Wu, S., Liu, Z. & Lau, N.-C. Contrasting circulation patterns of dry and humid heatwaves over southern China. *Geophys. Res. Lett.* **49**, e2022GL099243 (2022).
34. Deng, K., Yang, S., Gu, D., Lin, A. & Li, C. Record-breaking heat wave in southern China and delayed onset of South China Sea summer monsoon driven by the Pacific subtropical high. *Clim. Dyn.* **54**, 3751–3764 (2020).
35. Davenport, F. V. & Diffenbaugh, N. S. Using machine learning to analyze physical causes of climate change: a case study of U.S. midwest extreme precipitation. *Geophys. Res. Lett.* **48**, e2021GL093787 (2021).
36. Jiang, S., Zheng, Y., Wang, C. & Babovic, V. Uncovering flooding mechanisms across the contiguous united states through interpretive deep learning on representative catchments. *Water Resour. Res.* **58**, e2021WR030185 (2022).
37. Kondylatos, S. et al. Wildfire danger prediction and understanding with deep learning. *Geophys. Res. Lett.* **49**, e2022GL099368 (2022).
38. Xu, H. et al. Machine learning coupled structure mining method visualizes the impact of multiple drivers on ambient ozone. *Commun. Earth Environ.* **4**, 265 (2023).
39. Lin, W., Chen, R., Wen, Z. & Chen, W. Large-scale circulation features responsible for different types of extreme high temperatures with extreme coverage over South China. *Int. J. Climatol.* **42**, 974–992 (2022).
40. Li, X., Hu, Z.-Z., Liu, Y., Liang, P. & Jha, B. Causes and Predictions of 2022 Extremely Hot Summer in East Asia. *J. Geophys. Res. Atmo.* **128**, e2022JD038442 (2023).
41. Li, M., Luo, D., Yao, Y. & Zhong, L. Large-scale atmospheric circulation control of summer extreme hot events over China. *Int. J. Climatol.* **40**, 1456–1476 (2020).
42. Qianrong, M. et al. Possible influences of spring barents sea ice shrinking on chinese heat wave events. *Int. J. Climatol.* **43**, 6101–6113 (2023).
43. Wang, P. et al. Heat waves in China: definitions, leading patterns, and connections to large-scale atmospheric circulation and SSTs. *J. Geophys. Res. Atmos.* **122**, 10,679–610,699 (2017).
44. Fang, X., Zhang, J. & Hu, R. Antarctic warming induced South Atlantic warming effect on the heatwaves in East Asia in 2022. *Clim. Dyn.* **62**, 10247–10263 (2024).
45. Wazneh, H., Gachon, P., Laprise, R., de Vernal, A. & Tremblay, B. Atmospheric blocking events in the North Atlantic: trends and links to climate anomalies and teleconnections. *Clim. Dyn.* **56**, 2199–2221 (2021).
46. Yu, R. & Zhai, P. Changes in summer persistent precipitation over the middle-lower reaches of the yangtze river and associated atmospheric circulation patterns. *J. Meteorol. Res.* **35**, 393–401 (2021).
47. Steele, M., Ermold, W., Zhang J. Arctic ocean surface warming trends over the past 100 years. *Geophys. Res. Lett.* **35**, (2008).
48. Luo, B. et al. Rapid summer Russian Arctic sea-ice loss enhances the risk of recent Eastern Siberian wildfires. *Nat. Commun.* **15**, 5399 (2024).
49. Chen, X., Dai, A., Wen, Z. & Song, Y. Contributions of Arctic Sea-Ice loss and East Siberian Atmospheric blocking to 2020 record-breaking Meiyu-Baiu rainfall. *Geophys. Res. Lett.* **48**, e2021GL092748 (2021).
50. Nakamura, T. & Sato, T. A possible linkage of Eurasian heat wave and East Asian heavy rainfall in Relation to the Rapid Arctic warming. *Environ. Res.* **209**, 112881 (2022).
51. Francis, J. A., Vavrus, S. J. Evidence linking Arctic amplification to extreme weather in mid-latitudes. *Geophys. Res. Lett.* **39**, (2012).
52. Yang, X. et al. Interdecadal Variations of Different Types of Summer Heat Waves in Northeast China Associated with AMO and PDO. *J. Clim.* **34**, 7783–7797 (2021).
53. Chen, T. & Yoon, J. Interdecadal variation of the North Pacific wintertime blocking. *Mon. Wea Rev.* **130**, 3136–3143 (2002).

54. Zhu, Y., Wang, H., Zhou, W. & Ma, J. Recent changes in the summer precipitation pattern in East China and the background circulation. *Clim. Dyn.* **36**, 1463–1473 (2011).
55. Wei, J., Han, W., Wang, W., Zhang, L. & Rajagopalan, B. Intensification of heatwaves in China in recent decades: Roles of climate modes. *npj Clim. Atmos. Sci.* **6**, 98 (2023).
56. Luo, M. & Lau, N.-C. Heat waves in Southern China: synoptic behavior, long-term change, and urbanization effects. *J. Clim.* **30**, 703–720 (2017).
57. Wu, X. et al. Quantitatively evaluating the effect of urbanization on heat waves in China. *Sci. Total Environ.* **731**, 138857 (2020).
58. Mekis, É, Vincent, L. A., Shephard, M. W. & Zhang, X. Observed trends in severe weather conditions based on humidex, wind chill, and heavy rainfall events in Canada for 1953–2012. *Atmos.-Ocean* **53**, 383–397 (2015).
59. Zhang, W. et al. Assessing the impact of humidex on HFMD in Guangdong Province and its variability across social-economic status and age groups. *Sci. Rep.* **6**, 18965 (2016).
60. Zhao, R. et al. The exposure-response association between humidex and bacillary dysentery: A two-stage time series analysis of 316 cities in mainland China. *Sci. Total Environ.* **797**, 148840 (2021).
61. Wu, J. & Gao, X. A gridded daily observation dataset over China region and comparison with the other datasets. *Chin. J. Geophys.* **56**, 1102–1111 (2013).
62. Hersbach, H. et al. The ERA5 global reanalysis. *Q. J. R. Meteorol. Soc.* **146**, 1999–2049 (2020).
63. GPWv4 CFIESIN-C-CU. Gridded population of the world, version 4 (GPWv4): population density, Revision 11. (ed Palisades NSDaACS). Version 4.11 (2017).
64. Tibaldi, S., Molteni, F. On the operational predictability of blocking. *Tellus A: Dyn. Meteorol. Oceanogr.* **42**, 343–365 (1990).
65. Cheung, H. N., Zhou, W., Mok, H. Y. & Wu, M. C. Relationship between Ural–Siberian blocking and the East Asian winter monsoon in relation to the Arctic oscillation and the El Niño–Southern oscillation. *J. Clim.* **25**, 4242–4257 (2012).
66. Shi, N., Tajie, S., Tian, P., Wang, Y. & Wang, X. Contrasting relationship between wintertime blocking highs over Europe–Siberia and temperature anomalies in the Yangtze River basin. *Mon. Weather Rev.* **148**, 2953–2970 (2020).
67. Brunner, L., Hegerl, G. C. & Steiner, A. K. Connecting atmospheric blocking to european temperature extremes in spring. *J. Clim.* **30**, 585–594 (2017).
68. Cheung, H. N. et al. Observational climatology and characteristics of wintertime atmospheric blocking over Ural–Siberia. *Clim. Dyn.* **41**, 63–79 (2013).
69. Montavon, G., Samek, W. & Müller, K.-R. Methods for interpreting and understanding deep neural networks. *Digit. Signal Process.* **73**, 1–15 (2018).
70. Hilburn, K. A., Ebert-Uphoff, I. & Miller, S. D. Development and interpretation of a neural-network-based synthetic radar reflectivity estimator using GOES-R satellite observations. *J. Appl. Meteorol. Climatol.* **60**, 3–21 (2021).

Acknowledgements

This work was supported by the Guangdong Major Project of Basic and Applied Basic Research (Grant no. 2020B0301030004).

Author contributions

X.H. conceived the study, performed the analysis, and drafted the initial manuscript in collaboration with J.L. All authors contributed to the interpretation of the results and the final manuscript revision.

Competing interests

The authors declare no competing interests.

Additional information

Supplementary information The online version contains supplementary material available at https://doi.org/10.1038/s41612-025-01229-z.

Correspondence and requests for materials should be addressed to Jiandong Li.